


Article

The evolution of internal damage identified by means of X-ray computed tomography in two steels and the ensuing relation with Gurson's numerical modelling

Fernando Suárez ¹, Federico Sket ², Jaime C. Gálvez ^{3*}, David A. Cendón ⁴, José M. Atienza ⁴ and Jon Molina-Aldareguia ²

¹ Departamento de Ingeniería Mecánica y Minera, Universidad de Jaén, 23071 Jaén, Spain; fsuarez@ujaen.es

² Instituto IMDEA Materiales, C/ Eric Kandel 2, Tecnogetafe 28906 Madrid, Spain; federico.sket@imdea.org; jon.molina@imdea.org

³ Departamento de Ingeniería Civil-Construcción, Universidad Politécnica de Madrid, E.T.S.I. Caminos, Canales y Puertos, 28040 Madrid, Spain; jaime.galvez@upm.es

⁴ Departamento de Ciencia de Materiales, Universidad Politécnica de Madrid, E.T.S.I. Caminos, Canales y Puertos, 28040 Madrid, Spain; david.cendon.franco@upm.es; josemiguel.atienza@upm.es

* Correspondence: jaime.galvez@upm.es; Tel.: +034-913-365-350

Abstract: This paper analyses the evolution of the internal damage in two types of steel that show different fracture behaviours, with one of them being the initial material used for manufacturing prestressing steel wires, which shows a flat fracture surface perpendicular to the loading direction, and the other one being a standard steel used in reinforced concrete structures, which shows the typical cup-cone surface. 3mm-diameter cylindrical specimens are tested with a tensile test carried out in several loading stages and, after each of them, unloaded and analysed with X-ray tomography, which allows detection of internal damage throughout the tensile test. In the steel used for reinforcement, damage is developed progressively in the whole specimen, as predicted by Gurson-type models, while in the steel used for manufacturing prestressing steel-wire damage is developed only in the very last part of the test. In addition to the experimental study, a numerical analysis is carried out by means of the finite element method by using a Gurson model to reproduce the material behaviour.

Keywords: Steel, Tensile Test, XRCT, Damage Evolution, Gurson Model

1. Introduction

Steel is, with concrete, the most important building material used at the time, and the standard tensile test is the most widely used method to determine its principal material properties [1]. With it, the stress-strain curve of the material may be obtained before the ultimate tensile strength is reached; stresses and strains are then difficult to estimate. This is why the material behaviour after the ultimate tensile strength is usually neglected. Nevertheless, understanding the fracture mechanisms that lead to the eventual failure is of significant interest, since it can help to improve structural safety strategies.

The fracture of ductile materials has usually been explained with the theory of nucleation, growth and coalescence of microvoids [2]. According to this theory, at a first stage and with high loading being applied, microvoids are developed inside the material (nucleation) due to a decohesive process of small inclusions that are torn apart from the rest of the material or by the fracture of the particle that constitutes the inclusion itself. At a second stage, and under higher strain states, these microvoids increase their size (growth) until they become interconnected (coalescence). Such a process weakens the material until its eventual failure.

This theory has given rise to many mathematical models, with a special mention to Gurson-type models [3]. Since its appearance, the Gurson model has been applied to reproduce damage evolution in different ductile materials, such as aluminium, copper and steel [4–6]. Subsequent evolution of the model have been able to reproduce not only softening due to the growth of microvoids, but also the

eventual fracture of the material [7]. When such a model is applied to reproduce a tensile test on a ductile material, the damage begins to develop in very early stages of the test, as shown in Figure 1.

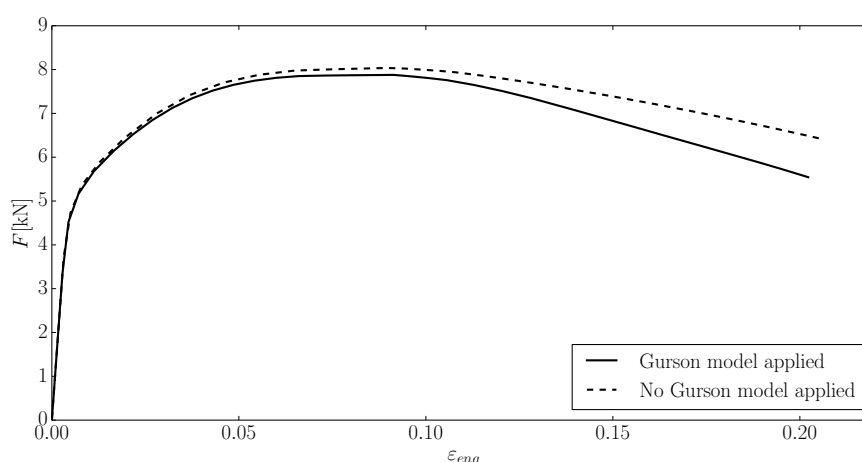


Figure 1. F- ϵ curves obtained with numerical simulations of the same specimen. One of them using a Gurson model and the other one without it.

Steel properties may differ depending on many factors, such as the chemical composition and the manufacturing process used. Such differences may affect ductility and the fracture mechanisms that lead to failure, with geometrically identical cylindrical specimens of different steels presenting a contrasting fracture surface after a tensile test. Figure 2 shows the fracture surface of two 9mm-diameter specimens made of different steels. The one on the left shows a typical cup-cone fracture, usually observed on ductile materials [2] and which belongs to a specimen made of standard steel used in reinforced concrete structures. The one on the right shows a flat fracture surface, where a dark circular region can be observed, belonging to a specimen made of steel used for manufacturing prestressing steel wires.

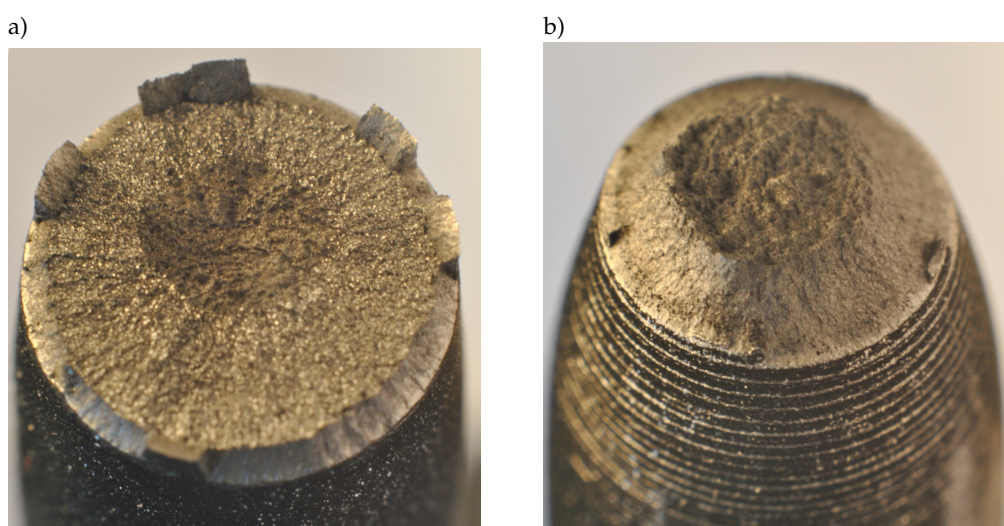


Figure 2. Fracture surfaces on 9mm-diameter specimens of two steels with different fracture patterns after testing under tension: a) Material 1; b) Material 2 [8].

In this work, two steels that have distinct fracture behaviours are analysed, with one of them being the initial material used to manufacture prestressing steel wires (Material 1), which exhibits the flat fracture pattern shown in Figure 2a and the other one a standard steel used in reinforced concrete structures (Material 2), with a fracture surface corresponding to the classical cup-cone shape (Figure

2b). These materials have been analysed in the past and their mechanical properties are well known; for further information, the reader is referred to [8] and [9]. In the first place, the fracture surfaces of both materials are observed with a scanning electronic microscope to identify the fracture mechanisms that take place. In the second place, an analysis of damage evolution along a tensile test on cylindrical steel specimens is carried out; this analysis is performed for both materials. Specimens are tested in subsequent loading stages and, at the end of each stage, analysed with X-ray computed tomography (XRCT) in order to identify the evolution of the internal damage. Maire et al. ([10–12]) have used a similar approach on aluminium and steel specimens to quantify damage evolution and study the effect of distinct triaxiality states on this process, which has served to compare experimental values of void growth and damage evolution with those predicted by numerical models.

In order to study how one of the most extended numerical models used with metals, the Gurson model, reproduces damage evolution, both tests are numerically reproduced. This numerical study is carried out using the finite element method and the material behaviour is reproduced by the Gurson model. The model is calibrated by using macroscopic results obtained experimentally: the load-strain curve and the necking radius evolution. The evolution of the internal porosity numerically obtained is compared with the experimental values provided by XRCT.

2. Experimental work

2.1. Materials

Two different steels are considered in this work. This section describes their characteristics.

2.1.1. Material 1

In the manufacturing process to obtain steel wires, raw eutectoid steel bars are cold-drawn, reducing their section by pulling them through a conical die. This process affects the failure behaviour of the material [13,14] and may introduce additional uncertainties in this study. Therefore, for this research, specimens of Material 1 were obtained from raw eutectoid pearlitic steel bars used for manufacturing prestressing steel wires. That is to say, they had not been affected by cold-drawing so the material was as isotropic as possible. The chemical composition of this material can be consulted in Table 1. According to the metallographic analysis, the microstructure of this material is formed by perlite, with a lamellar structure of equi-axed grains with an average size of $G=9$. This microstructure can be seen in Figure 3a.

Table 1. Chemical composition of both materials in %.

Material	C	Si	Mn	P	S	Cr	Mo
1	0.83	0.25	0.72	0.012	0.004	0.24	<0.01
2	0.22	0.18	1.00	0.024	0.042	0.08	0.03

Material	Ni	Cu	Al	Ti	Nb	V	N
1	0.02	0.01	<0.003	<0.005	<0.005	<0.01	0.0097
2	0.14	0.46	<0.003	<0.005	<0.005	<0.01	0.0113

2.1.2. Material 2

Specimens of Material 2 are made of steel reinforcement B 500 C, according to the European Standard EN 10020 [15], with high ductility and an elastic limit f_t of 500N/mm². The chemical composition of this material can be consulted in Table 1. According to the aforementioned metallographic analysis, the microstructure of this material is formed by ferrite and perlite in a proportion of 50/50, with the perlite being sorbitic and equi-axed grains with an average size of $G=9$. This microstructure can be seen in Figure 3b.

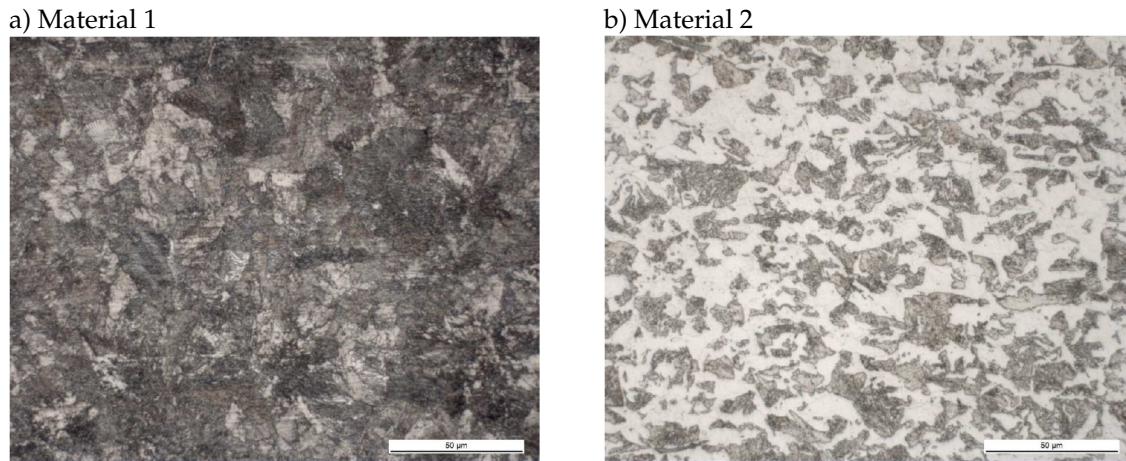


Figure 3. Microstructure of both materials in the longitudinal direction before testing.

2.2. Specimens

Two diameters were considered for each material: 3mm and 9mm. The 9mm-diameter specimens were used to analyse the fracture surfaces, since comparison is easier in specimens with larger cross sections. The 3mm-diameter specimens were used in the damage evolution analysis to ensure a correct penetration of the X-rays used to identify the internal damage. The dimensions of these specimens can be checked in Figure 4.

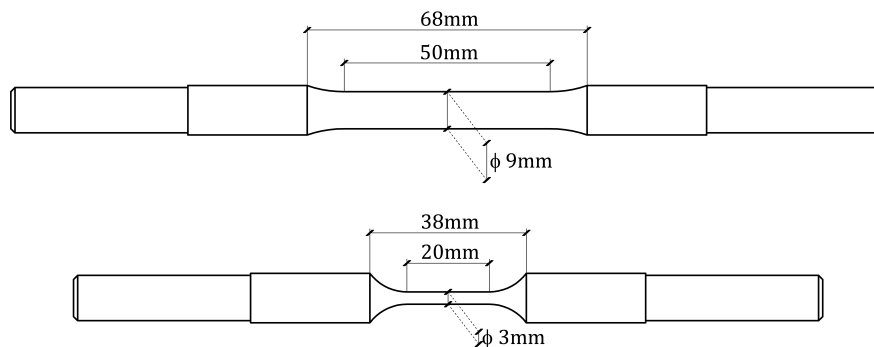


Figure 4. Specimens dimensions.

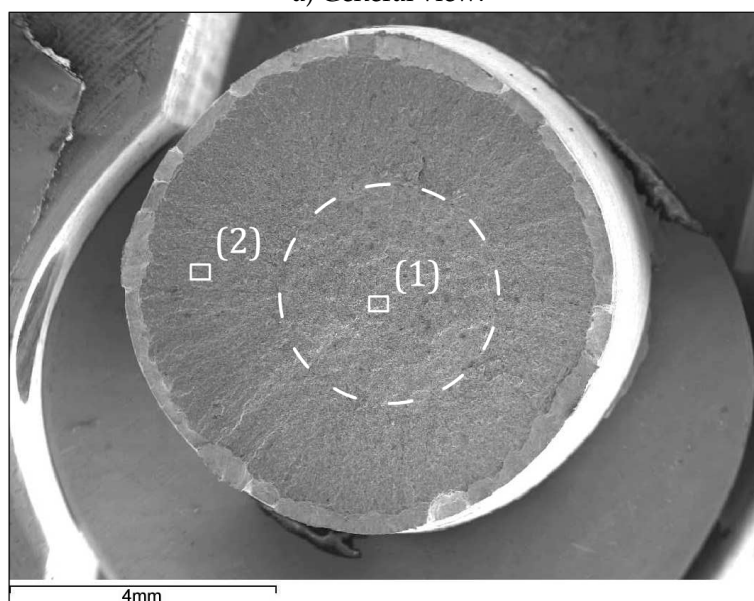
2.3. Testing procedure used to study the damage evolution

In order to follow the damage evolution inside a specimen, it was tested in subsequent load stages, after each of which the specimen was unloaded and its neck analysed with X-ray computed tomography (Nanotom 160NF, Phoenix). The steps given for each analysis are given as follows:

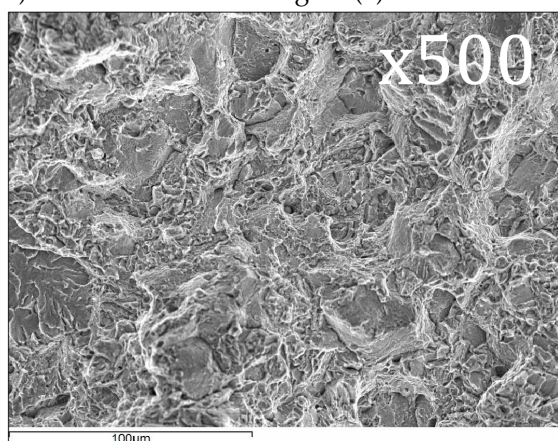
1. X-ray tomographic analysis before the specimen is tested.
2. Specimen is tested until the maximum load is reached; then, it is unloaded.
3. X-ray tomographic analysis after the first stage.
4. Specimen is tested until the second stage is reached; then, it is unloaded.
5. X-ray tomographic analysis after the second stage.
6. The previous steps are followed until the point of failure.

The tensile tests were carried out with a Suzpecar universal testing machine and a load cell of 100kN. Every load stage was performed with a displacement control, and at a very low speed of displacement of the clamping jaws (of the order of 0.05 mm/min in the last stages), to avoid dynamic effects during the test. The tomographic images were collected at 80kV and 140µA by using a tungsten target.

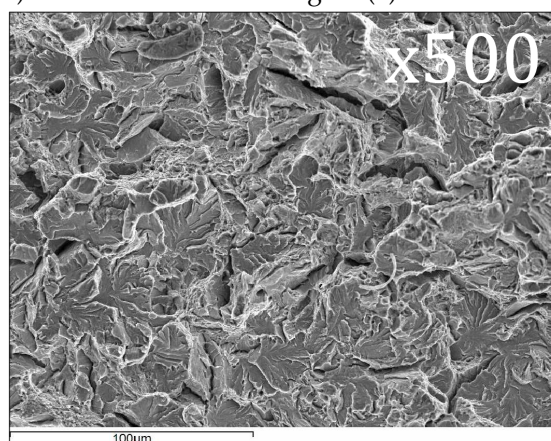
a) General view:



b) Detail of the central region (1):



c) Detail of the external region (2):

**Figure 5.** Fractographs obtained from the 9mm-diameter specimen made of Material 1.

2.4. Results

2.4.1. Fractographic analysis of the fracture surfaces

Figure 5 and Figure 6 show the fractographs obtained with the 9mm-diameter specimens tested, with the former corresponding to the Material 1 specimen and the latter to the Material 2 specimen. For each of them, a general fractograph of the fracture surface and two closer fractographs are shown, one of the central region of the surface and the other of the external region. The internal region is highlighted by a dotted circumference. In the Material 1 specimen it corresponds to the internal dark region observed after a tensile test and in the Material 2 it corresponds to the flat surface perpendicular to the specimen axis in a cup-cone fracture surface.

The fractographic pictures of the Material 1 specimen show that the central region presents a surface with dimples, different from that of the external region, where sharper edges are noticed. According to this, the central region fails by means of a nucleation, growth and coalescence mechanism, while the external region corresponds to a cleavage fracture mechanism. In the case of the Material 2 specimen, the central region presents a high number of voids and evident dimples, which corresponds to a clear nucleation, growth and coalescence mechanism. The external region presents fewer voids and

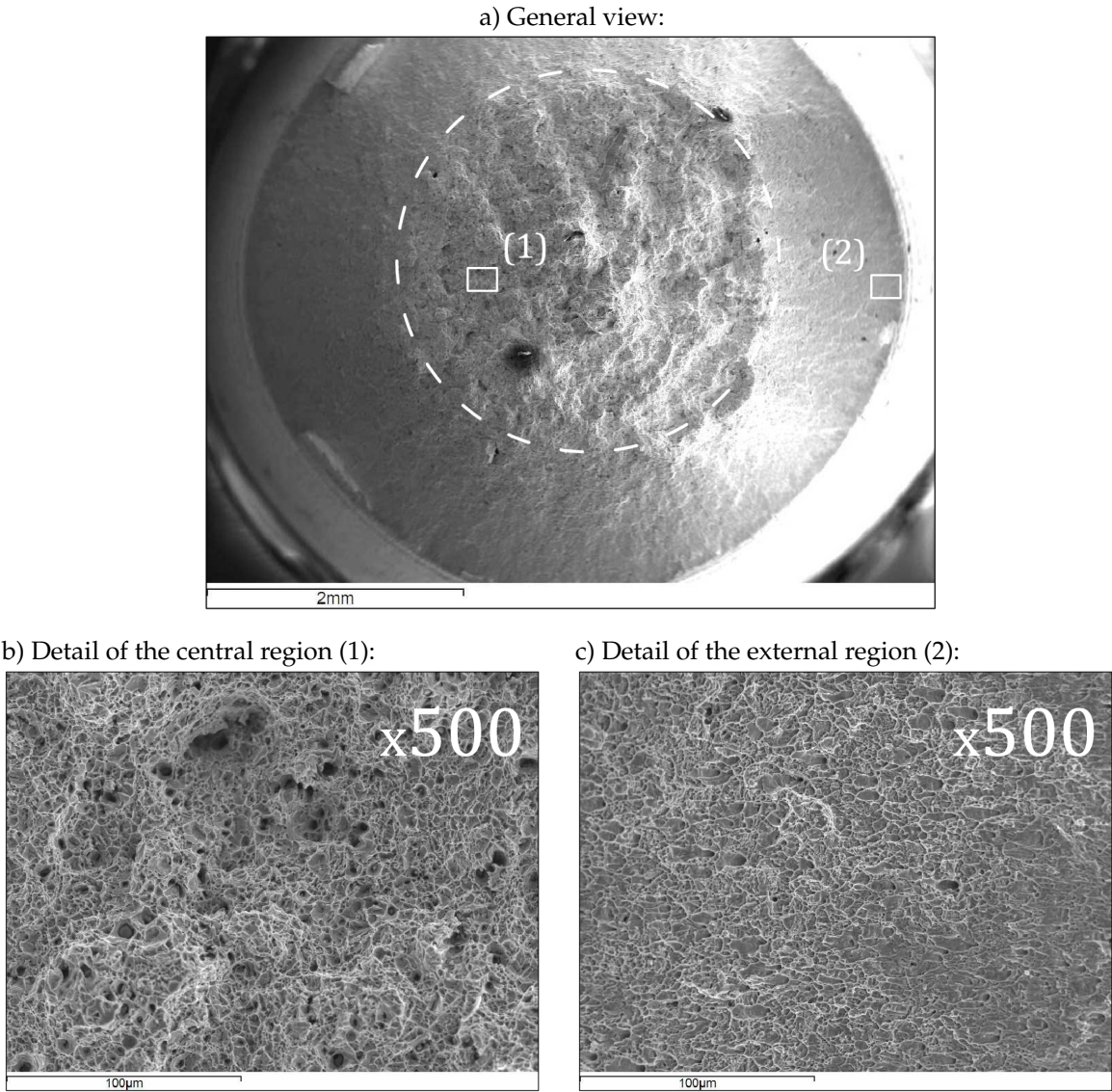


Figure 6. Fractographs obtained from the 9mm-diameter specimen made of Material 2.

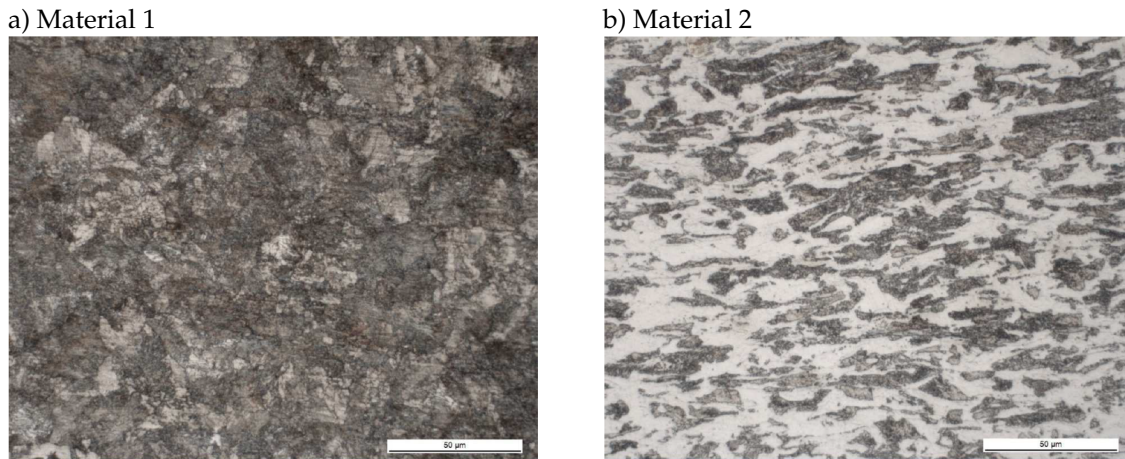


Figure 7. Microstructure of both materials in the longitudinal direction after testing.

slightly sharp edges, which seems to indicate a combination of the nucleation, growth and coalescence mechanism with the cleavage mechanism.

2.4.2. Metallographic analysis after the test

Figure 7 shows the microstructure in the longitudinal direction of Material 1 and Material 2 after the test in the necking region.

In the case of Material 1, raw eutectoid pearlitic steel, no differences can be observed when compared with the microstructure before testing (see Figure 3a). In the case of Material 2, standard steel used as reinforcement in concrete structures, grains are oriented in the longitudinal direction after the test and show a shape factor of $f_{sh} = 4$.

2.4.3. Internal damage evolution analysis

This analysis was performed with 3mm-diameter specimens to allow penetration of X-rays into the material. Since XRCT is an expensive technique that requires much postprocessing work, only one specimen for each material is analysed, which is usual practice when this technique is applied [16–18]. The analysis was carried out with a voxel size of $2.5 \mu\text{m}$ (Nanotom 160 NF, from Phoenix X-ray). As mentioned before, to carry out this analysis the tensile tests were performed in subsequent load stages. These stages are defined by the engineering strain developed along an initial length of 12.5mm and can be consulted in Table 2. Figure 8 shows them over the corresponding $F-\varepsilon_{eng}$ curves. Note that this figure shows the experimental results for both analysed materials compared with the numerical results that will be described later.

Table 2. Stages used for the damage evolution analysis with the specimens of both materials. Engineering strain over a 12.5mm initial length is used for identifying every stage.

Stage	1	2	3	4	5
Material 1	0.076	0.104	0.118	0.128	—
Material 2	0.193	0.267	0.288	0.306	0.319

Figure 9 presents the results for the Material 1 specimen. Results are given for the specimen before testing and for each of the four stages considered. Three pictures are shown for each stage: a longitudinal section of the necking region, a projection of damage on the cross section and a perspective of the internal damage in the necking region.

According to these results, nucleation and growth of microvoids is unnoticeable in the first stage, which corresponds to the maximum load instant. In the second and third stages, the mechanism of nucleation and growth of microvoids can be clearly observed, though it is not until the fourth stage that an evident internal damage is developed. Therefore, according to the theory of nucleation, growth

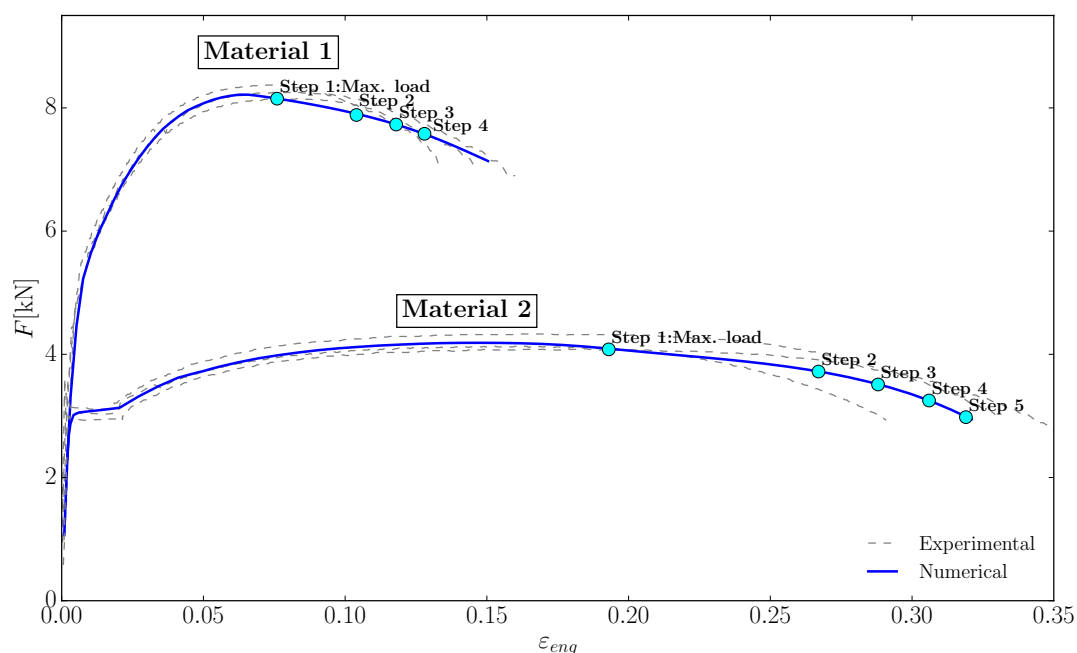


Figure 8. Load-strain curve of the 3mm-diameter specimen of both materials; comparison between the experimental results and the numerical models. The stages used for the damage evolution analysis are represented with blue circles (the engineering strain has been obtained using an initial gauge length of 12.5 mm).

and coalescence of microvoids, as the test progresses the microvoids start to appear and grow in an even manner but the internal damage that leads the specimen to failure only appears at the very end of the test.

Figure 10 shows the results for the Material 2 specimen. As in the Material 1 specimen, results are given for before testing and for each of the stages considered, five in this case; and, as in Figure 9, three pictures are shown for each of them: a longitudinal section of the necking region, a projection of damage on the floor plan and a perspective of the internal damage in the necking region.

As in the Material 1 specimen, the mechanism of nucleation and growth of voids is clearly noticeable: as the test progresses, evenly spaced voids start to appear and grow.

2.4.4. Longitudinal and radial distribution of voids at each stage

In order to understand how voids nucleate and grow inside the specimen during the test, their distribution has been obtained in the longitudinal direction and in the radial direction for each stage. In the longitudinal direction, the specimen part considered was 3.5mm long centered at the necking area and the void volume was measured for 0.025mm-long slices. In the radial direction the volume was measured at seven concentric hollow cylinders (except the smaller one, which was a full cylinder) of the same volume; this measurement was obtained for 349 slices, 0.8725mm in length. To do this work, the raw data obtained with XRCT was filtered by means of Matlab® scripts and functions [19].

2.5. Discussion on the experimental data

The fractographs obtained with the 9mm-diameter specimens (Figures 5 and 6) show two clearly different fracture behaviours between Material 1 and Material 2. While the former presents two clearly defined failure mechanisms, nucleation and growth of microvoids in the internal region and cleavage in the external one, the latter presents a global nucleation, growth and coalescence mechanism all over the surface and a combination of this mechanism with a slight cleavage only in the very external part of the inclined plane of the cup-cone shape. This last observation agrees with previous research published by Scheider and Brocks [20] or by Suárez et al., [8] and [9].

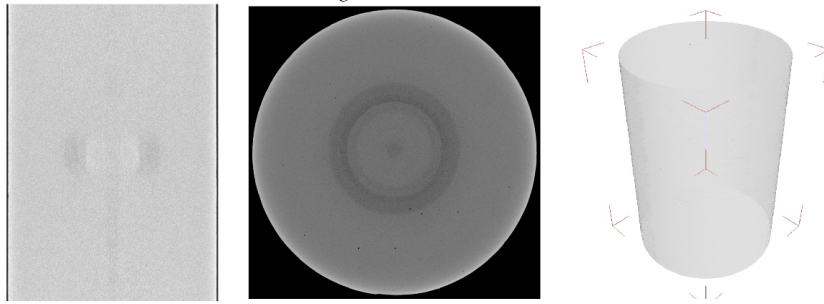
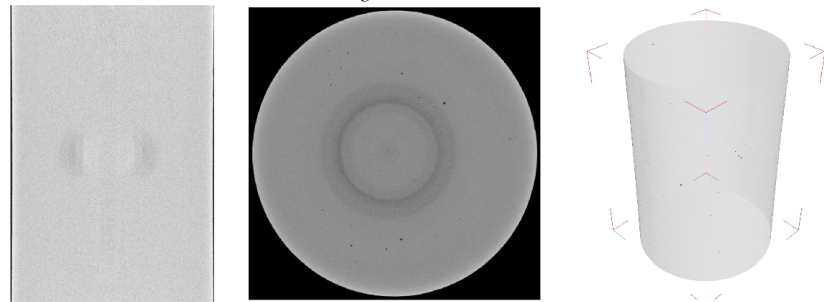
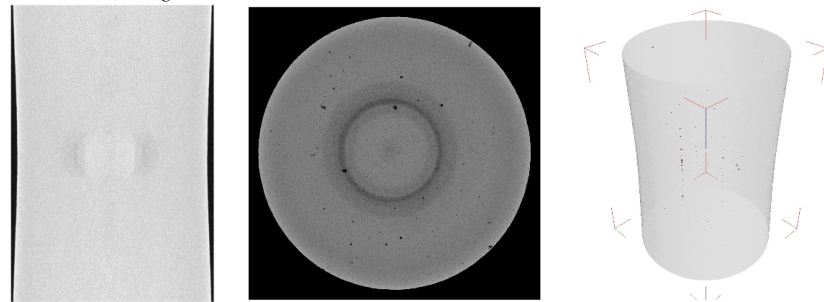
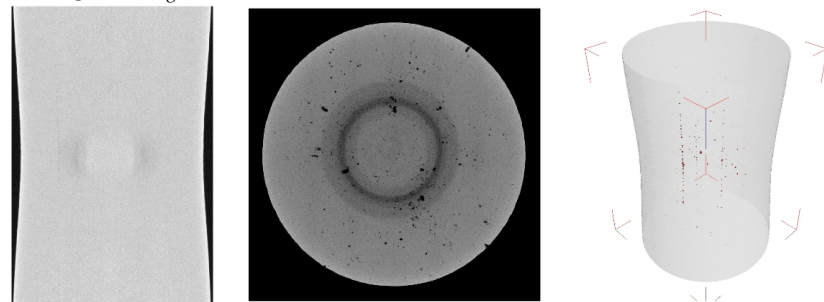
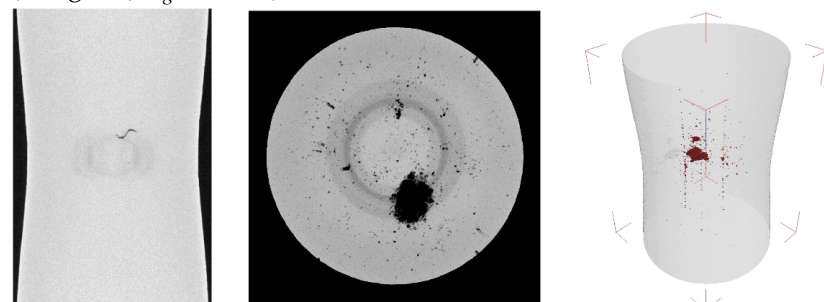
a) Stage 0: Before testing ($\epsilon_{eng} = 0$)b) Stage 1: Maximum load ($\epsilon_{eng} = 0.076$)c) Stage 2 ($\epsilon_{eng} = 0.104$)d) Stage 3 ($\epsilon_{eng} = 0.118$)e) Stage 4 ($\epsilon_{eng} = 0.128$)

Figure 9. Results of the XRCT analysis of the necking zone for Material 1. For each stage, three results are given: I) Longitudinal section, II) Damage projected on the floor plane and III) Perspective of the internal damage.

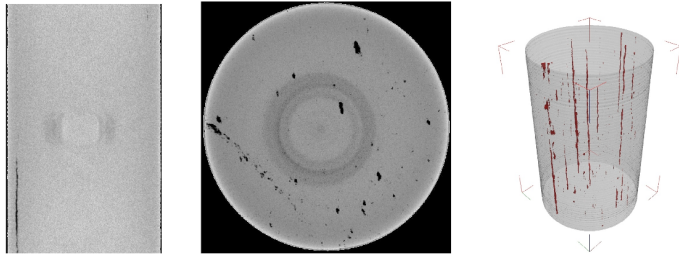
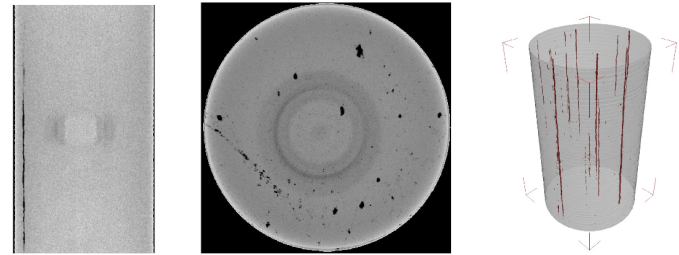
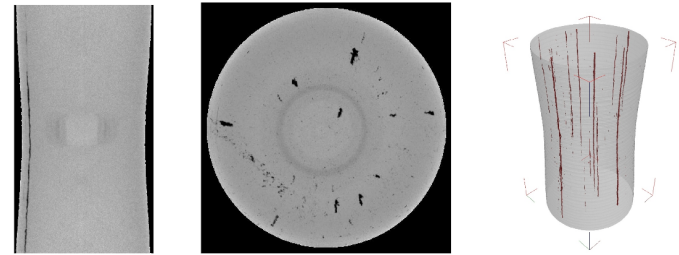
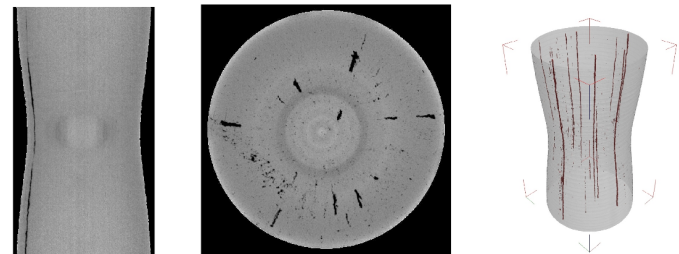
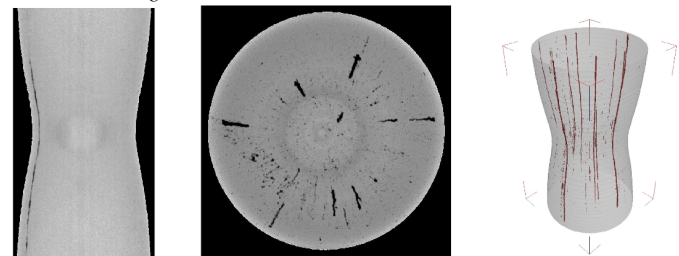
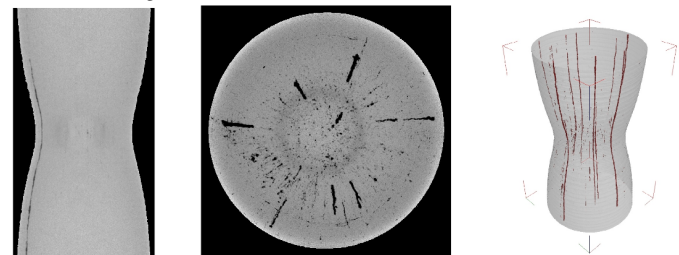
a) Stage 0: Before testing ($\epsilon_{eng} = 0$)b) Stage 1: Maximum load ($\epsilon_{eng} = 0.193$)c) Stage 2 ($\epsilon_{eng} = 0.267$)d) Stage 3 ($\epsilon_{eng} = 0.288$)e) Stage 4 ($\epsilon_{eng} = 0.306$)f) Stage 5 ($\epsilon_{eng} = 0.319$)

Figure 10. Results of the XRCT analysis of the necking zone for Material 2. For each stage, three results are given: I) Longitudinal section, II) Damage projected on the cross section and III) Perspective of the internal damage.

Therefore, while the fracture surface of Material 2 and its cup-cone shape agrees with the observations by Bluhm and Morrissey [21] and suggests a clearly ductile behaviour along the test, the fracture surface of Material 1 shows a different fracture behaviour. It suggests that the internal damage, represented by the internal region, develops progressively and opens an internal crack until it eventually fails, propagating the internal crack outwards by a cleavage mechanism. Hence, Material 1 failure presents a brittle-ductile transition phenomenon.

As regards the tomographic images, the initial image obtained for both specimens, before testing, highlights the different nature of both materials. Material 1 has almost no internal voids, whereas Material 2 presents a high volume of them. It is interesting to observe how these voids are lined up longitudinally, which may be due to the manufacturing process.

The different nature of both materials can also be noticed looking at how differently they behave, not only in terms of stress but also in terms of strain; Material 1 has a maximum strain of around 0.13 at failure while Material 2 reaches a value of about 0.34. This is also evident given that necking is much more noticeable in Material 2 than in Material 1.

In Material 1, some small voids can be noticed under maximum loading. As strain increases, new voids appear, some in a random manner but others aligned in the loading direction. The most remarkable observation in this material entails the last stage, an instant very close to failure. Before this instant, voids appear somehow independently and not connected to each other, but at step four some internal cracks seem to have formed, especially a large one in the center of the necking region, generating a large plane crack. This observation agrees with the hypothesis posed in [8,9,22], suggesting that fracture is initiated by an internal crack that, once it reaches a certain size, acts as an internal notch that triggers a brittle fracture process. This is interesting since it allows the use of certain models from the field of linear elastic fracture mechanics which work reasonably well for a clearly elastic-plastic material.

In the case of Material 2, a high number of voids or inclusions is present before any load is applied. As load increases, the voids increase in number and volume. Different from Material 1, no void coalescence can be identified. It is unclear if this means that coalescence takes place just instants before failure or if the test could not be stopped close enough to failure, so internal fracture surfaces could be observed. According to the results reported by Bluhm and Morrissey [21], a fracture plane perpendicular to the loading direction could be expected, which would result in the flat surface of the cup-cone fracture pattern, and finally inclined fracture planes, which would result in the shear planes of the cup-cone shape.

Therefore, the internal damage evolution analysis confirms that, in the case of Material 2, failure is due to a generalised weakening process that takes place all over the cross section as a result of a nucleation, growth and coalescence of microvoids mechanism. In the case of Material 1, although this mechanism is also observed, the eventual failure of the specimen is provoked by an internal crack opening that takes place in the very late instant of the tensile test. This observation confirms that the failure of Material 1 presents a brittle-ductile transition phenomenon where the specimen shows a ductile behaviour until the internal crack is large enough to provoke an eventual brittle failure.

3. Numerical work

This section presents the numerical work carried out in this study. In order to analyse the numerical behaviour of the Gurson model, which is widely used for reproducing the material degradation in metals, the experimental data is compared with numerical simulations using this model. The tensile tests of both materials are reproduced numerically by means of the finite element method, using the implicit version of the commercial software Abaqus® [23].

3.1. Description of the finite element model

3.1.1. Geometry

Because of the axial symmetry of the problem, only 1/24th of each specimen has been considered, as shown in Figure 11. In order to force necking at the $x = 0$ plane, the specimen is not perfectly cylindrical, but its radius varies from 1.5mm at $x = 0$ to 1.51mm at $x = 7.25$ mm, enough to induce stress concentration numerically at $x = 0$. The mesh was defined after a mesh-size convergence study [22] and resulted in a mesh of 141378 elements shown in Figure 12. The length of the elements in the longitudinal direction in the necking region of the specimen was 0.094 mm.

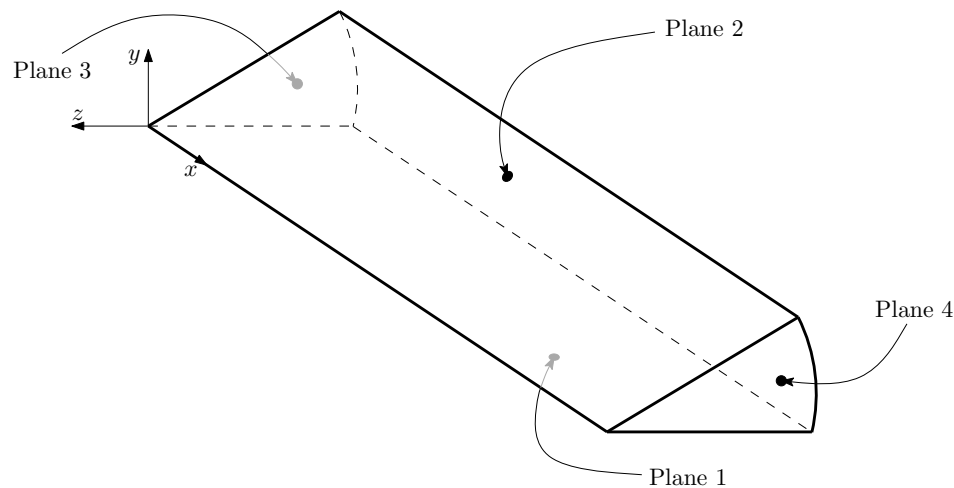


Figure 11. Description of the model. Plane 3 represents the eventual plane of failure; displacement is imposed in direction of the x axis on plane 4.

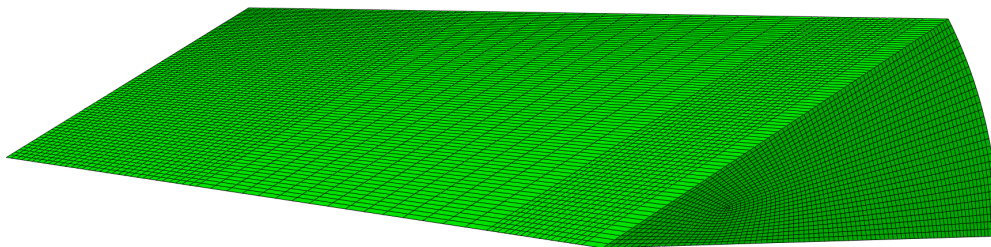


Figure 12. Mesh used to reproduce the experimental results.

3.1.2. Boundary conditions and load

The load is applied in the X -axis direction and the YZ plane represents the eventual plane of fracture. With regard to the boundary conditions, nodes on the $x = 0$ plane are constrained in the x direction, nodes on the xz plane (plane 1) are constrained only in the y direction and nodes on the inclined plane (plane 2) are constrained only perpendicularly to the plane.

The load is applied by defining an imposed displacement in the x direction to the nodes placed at $x = 7.25$ mm (plane 4).

3.1.3. Materials

The specimens are modelled with a porous elastic-plastic material that follows the Gurson's formulation available in Abaqus®.

The elastic-plastic behaviour of the latter has been defined by the $\sigma - \varepsilon$ curve obtained experimentally up to the maximum load point, the subsequent hardening slope is in principle unknown

and must be estimated. This has been done by using a parameter r which provides the slope after maximum loading as $r = \frac{\Delta\sigma}{\Delta\varepsilon}$.

However, the porous feature is modelled by a Gurson model, where the yield criterion is given by the expression (1).

$$\Phi = \left(\frac{q}{\sigma_y} \right)^2 + 2f \cosh \left(-\frac{3p}{2\sigma_y} \right) - (1 + f^2) = 0 \quad (1)$$

where p and q are the hydrostatic pressure and the von Mises equivalent stress, respectively and f is the void volume fraction.

3.2. Calibrated models

With the aforementioned description of the model, the following parameters can be identified for calibration:

- Material relative density, d . Please, note that here we follow the Gurson model parameters used in the implementation of the model available in Abaqus[®], therefore a value of $d = 1$ implies a fully dense material with an initial void volume fraction of $f = 0$.
- Hardening slope after the maximum load defined as a stress-strain ratio, r .
- Mean equivalent plastic strain for void nucleation, ε_N .
- Standard deviation of the distribution, s_N .
- Volumetric fraction of nucleated voids, f_N .

In order to calibrate both models, the numerical results are compared with the experimental data by means of two criteria. The load-strain curve must be similar enough and the evolution of the necking radius in the center of the neck must follow the same pattern as experimentally observed. Figures 8 and 13 show that both criteria are met for both models.

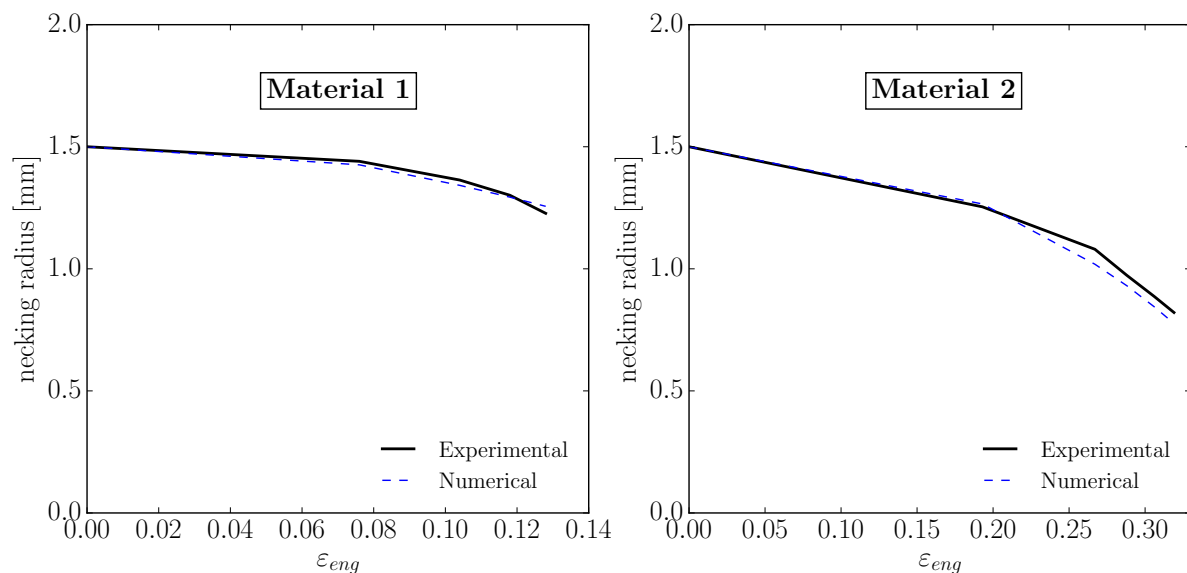


Figure 13. Necking radius evolution for both materials; numerical and experimental results are compared.

The calibration process was carried out by trial and error using around 50 different sets of parameters for each material. As a result of this process, the sets of parameters shown at Table 3 were obtained.

Table 3. Initial parameters for FEM models of both materials.

Material	E [N/mm ²]	ν	r	d	ε_N	s_N	f_N
1	160385	0.30	782	0.999	0.4	0.1	0.02
2	191536	0.30	762	0.99	0.3	0.1	0.06

3.2.1. Comparison with the experimental data

The calibration of both models ensures good agreement with the experimental data at the macroscopic level. Nevertheless, the interest in this study is to compare the evolution of porosity inside the material along the tensile test.

The XRCT technique provides information of the interior of the specimen in the form of voxels grouped in slices. That is to say, a slice is the group of voxels placed at the same longitudinal distance from the fracture plane, considered as the origin. To obtain the void volume fraction (VVF) longitudinal profiles with the experimental data, the porosity fraction is counted for each slice.

Regarding the VVF radial profiles, the void fraction is obtained for concentric cylindrical rings. The inner cylinder is full and the rest are hollow. Throughout this process, the measurement of internal porosity is carefully obtained, neglecting the internal fracture at step four in Material 1 and the longitudinal porosity chains in Material 2, which appear even in the initial tomography, taken before any load is applied.

The same procedure is followed to obtain the VVF longitudinal and radial profiles with the numerical models; to do this, the results obtained with Abaqus® are filtered by several Python-language scripts using NumPy and SciPy libraries [24–26] and the profiles are extracted for the same strain rates considered experimentally (see Table 2).

Figure 14 and Figure 15 compare the numerical and experimental profiles.

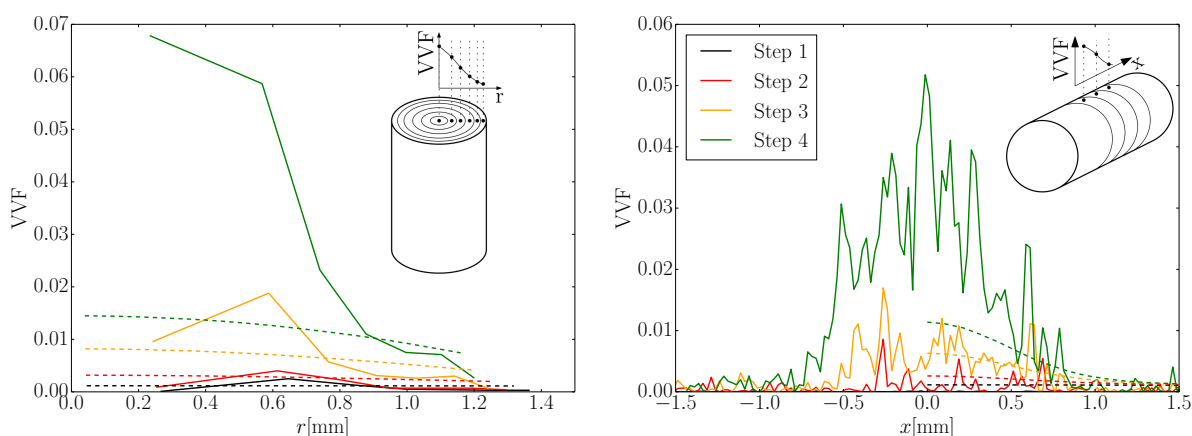


Figure 14. Radial and longitudinal voids distribution experimentally (continuous lines) and numerically (dashed lines) obtained for Material 1.

In both materials the longitudinal and radial profiles numerically obtained are somewhat different from the experimental ones.

In the case of Material 1 and regarding the longitudinal profile, these differences might not be so important and, probably, a different adjustment of the model parameters could provide a more similar final profile (green dashed line). Nevertheless, there is an interesting difference, since the experimental data suggest a high porosity development in the last part of the test, between steps 3 and 4; this is not observed in the numerical results. Regarding the radial profiles, two important differences can be highlighted: the high porosity increment experimentally observed between steps three and four is not obtained in the numerical model; the experimental profiles tend to have a steep slope around the middle of the radius, being almost zero at the external part of the specimen while the numerically

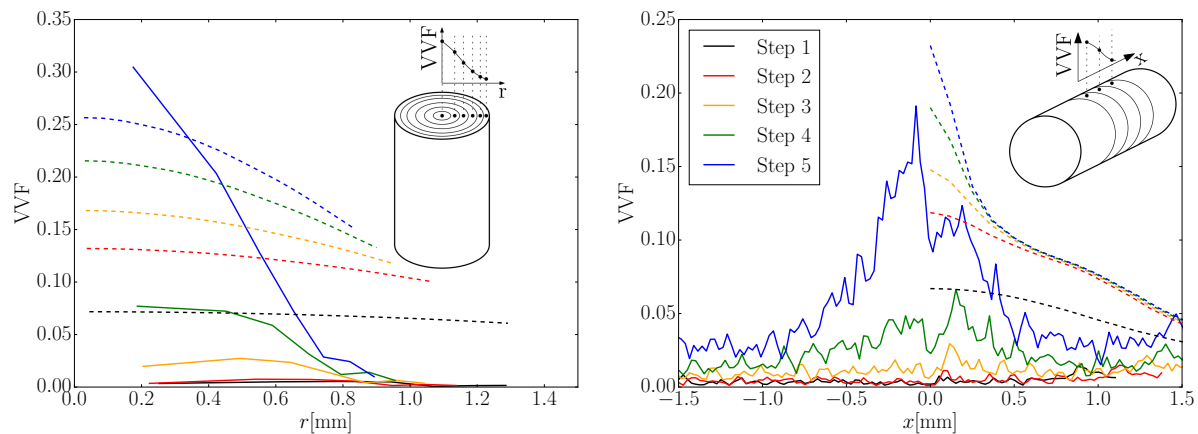


Figure 15. Radial and longitudinal voids distribution experimentally (continuous lines) and numerically (dashed lines) obtained for Material 2.

obtained profiles tend to be almost flat, even presenting a higher porosity in the external part of the specimen than that measured experimentally.

In the case of Material 2, both radial and longitudinal profiles may seem to be more similar to the experimental ones, since the porosity profiles for the last step are more similar than in the case of Material 1. Nevertheless, by taking a closer look at these profiles the same differences can be pointed out. In the case of the longitudinal profiles, although the last step profile may seem more or less similar to the experimental one, its evolution is different. For example, while the experimental profile does not develop much in the first two steps and only increases slightly in the steps three and four, the numerical profile develops much from the very first step. Again, as observed for Material 1, the high porosity increment observed experimentally in the last step is not obtained numerically. In the case of the radial profiles, the same differences observed for Material 1 can be identified, since all the numerical profiles are almost flat, different from the numerical ones, and there is not a high porosity evolution in the last step, as experimentally obtained.

From these results, it can be concluded that although a set of parameters provides a macroscopically correct response of the specimen, porosity evolution is different not only for Material 1, which could be expected since it is a steel with a little ductile response and a fracture pattern different from the cup-cone shape, but also for Material 2, which in principle is a material with a behaviour typically reproduced by Gurson-type models.

Nevertheless, it should be noted that in this work the original Gurson model has been used, thus it only reproduces the effects of nucleation and growth of voids, but not coalescence.

3.2.2. Mesh size effect on the voids volume profiles

Mesh density may have a strong influence on the numerical results, that is why, as already mentioned, the model has been calibrated using the load-strain curve and the necking evolution. However, there is still no data about how refining the mesh affects the evolution of volume profiles. To this respect, since the mesh is already pretty fine in the radial and angular directions as can be observed in Figure 12, with sides of around $20\ \mu\text{m}$ in length, only the longitudinal dimension of the elements has been taken into account.

For this study, several meshes have been generated using the same radial and angular discretization and using different element longitudinal lengths in the necking region l , ranging from a coarse mesh with $l = 0.75\text{mm}$. (Figure 16a)) to a fine mesh of $l = 0.075\text{mm}$. (Figure Figure 16b)).

Figures 17 and 18 show the radial and longitudinal distribution of each mesh at the last considered strain rate experimentally measured for each material (step 4 for Material 1 and step 5 for Material 2), which can be considered as the most representative of them all. In the Appendix at the end of this

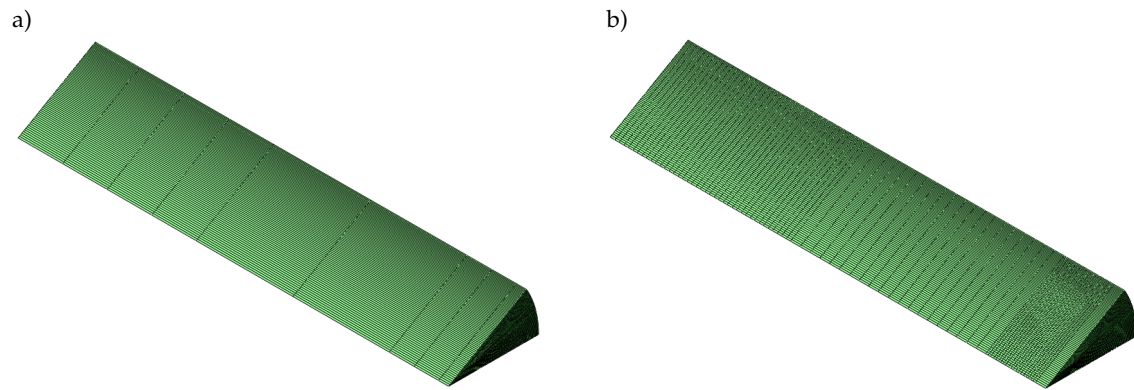


Figure 16. a) Coarser mesh with $l = 0.75\text{mm}$. and b) Finer mesh with $l = 0.075\text{mm}$.

article, the reader can find all the voids diagrams for each mesh and for all the strain rates considered in this study.

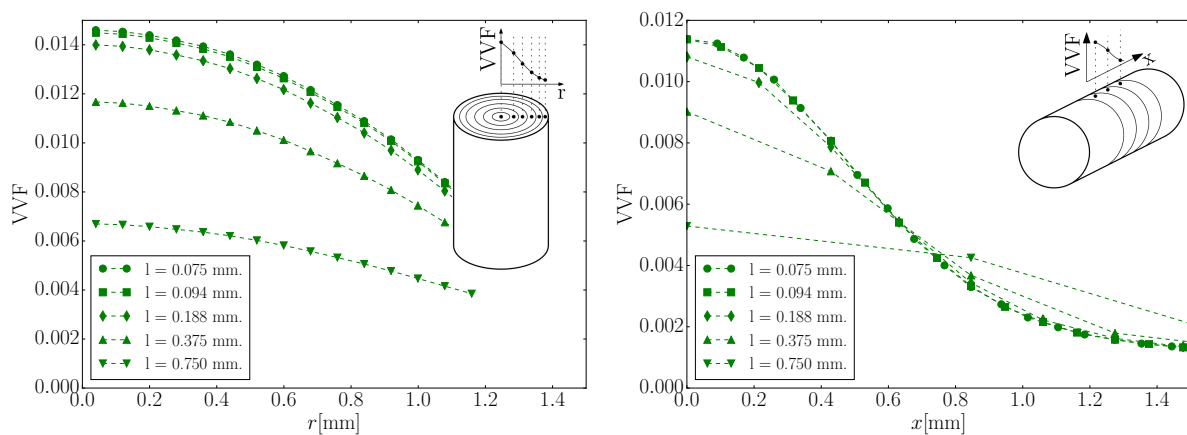


Figure 17. Radial and longitudinal voids distribution of a specimen of Material 1 at step 4 obtained using meshes with different element longitudinal lengths.

In both materials, mesh refinement leads to steeper shapes of both voids distribution, radial and longitudinal. Nevertheless, while in the case of Material 1 the second finer mesh ($l = 0.094\text{mm}$) seems to be fine enough (both diagrams are almost coincident with the finer mesh), in the case of Material 2, it seems that further refinement could lead to slightly steeper shapes of the diagram. This is interesting, since different calibration parameters of the Gurson model seem to require different mesh refinement when the voids distribution shapes are to be analysed.

4. Conclusions

In this paper, two steels with distinct fracture patterns have been analysed, with Material 1 corresponding to an eutectoid steel used for manufacturing prestressing steel wires and Material 2 being a standard steel used as reinforcement in concrete structures. The study has been carried out on 3 mm-diameter cylindrical specimens, tested under tension in subsequent incremental strain steps up to failure. The internal damage evolution has been identified by means of XRCT.

When a specimen of Material 1 is tested, the fracture surface is plane and perpendicular to the loading direction with two different regions: a central dark region and a brighter surrounding region. In the case of a specimen of Material 2, the fracture pattern corresponds to the cup-cone surface, extensively studied by many researchers.

The fractographic images obtained for both materials allow identification of the mechanism of nucleation, growth and coalescence of microvoids in each material. Material 1 has almost no initial voids and a slight internal porosity is developed through the test; the fracture presents a

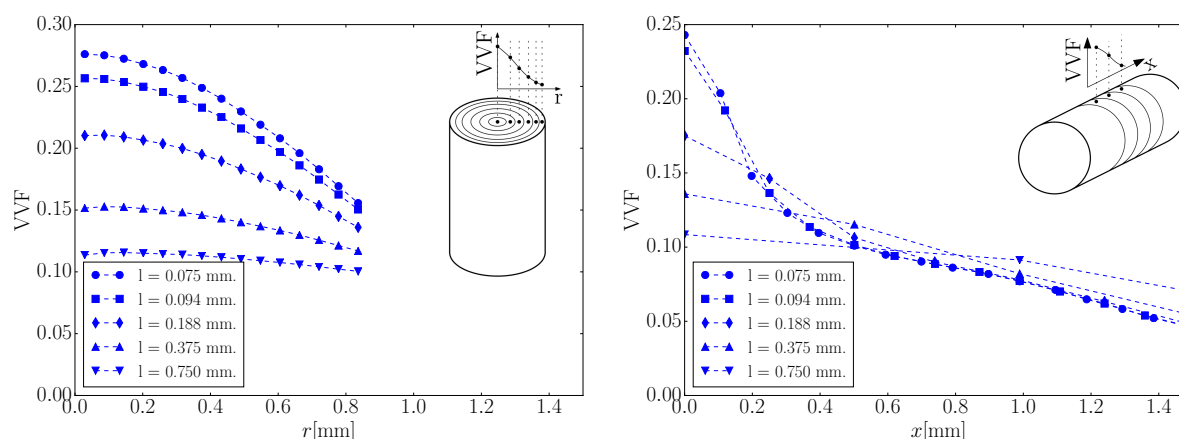


Figure 18. Radial and longitudinal voids distribution of a specimen of Material 2 at step 5 obtained using meshes with different element longitudinal lengths.

ductile-fragile transition phenomenon. As the test progresses, a ductile behaviour is observed where the nucleation and growth of microvoids mechanism is developed and, immediately before failure, a large penny-shaped internal crack, perpendicular to the loading direction, is formed. This leads to an eventual brittle fracture acting as an internal notch, which agrees well with previous works ([8,9]). Material 2 has an initial high volume of voids or inclusions, probably due to the manufacturing process, which increases as the tensile test is carried out. In this case the fracture is evenly developed over the whole cross section: the nucleation and growth of microvoids mechanism takes place evenly throughout the test and causes a progressive weakening of the material that does not provoke a critical internal crack. Although no internal fracture planes have been observed in Material 2, according to the observations by Bluhm and Morrissey in [21], the progressive formation of the cup-cone fracture surface should be expected. This could be due to a fast formation of this surface before fracture.

Since the Gurson model allows identification of the development of voids inside the material, the test has been numerically reproduced by means of finite element models by using a Gurson porous material. To calibrate the parameters for each material, two macroscopic values have been considered: the load-strain curve and the evolution of the necking radius. After calibration, internal porosity evolution has been compared with that obtained experimentally for both materials in the longitudinal and radial directions.

It is interesting to observe that, although the Gurson model is able to correctly reproduce the two macroscopic criteria used for calibration in both materials, internal porosity profiles differ considerably from the experimental ones. It is also interesting to observe that, when the void volume evolution is analysed, the numerical model calibration may require different mesh refinement for distinct set of calibrated parameters.

The use of a complete Gurson-Tvergaard-Needleman model [7], which includes additional material parameters to account for the effects of void interactions and consider the effect of void coalescence, could help to improve the comparison with the experimental results.

Author Contributions: Jaime C. Gálvez, José M. Atienza and David. A. Cendón conceived and designed the experimental work and supervised the numerical work; Fernando Suárez carried out the experimental work on the tensile testing; Fernando Suárez carried out the the numerical work that deals with the Gurson modelling under the supervision of David A. Cendón; Federico Sket and Jon Molina-Aldareguia carried out the XRCT analysis; Fernando Suárez wrote the paper.

Funding: This research was funded by the Spanish Ministry of Economy, Industry and Competitiveness by means of the Research Fund Project BIA 2016 78742-C2-2-R.

Acknowledgments: The authors want to express their gratitude to Luis del Pozo and Luisa Villares, from Emesa Trefilería, S.A. (Arteixo, La Coruña) for supplying the steel wires, as well as for providing their useful comments.

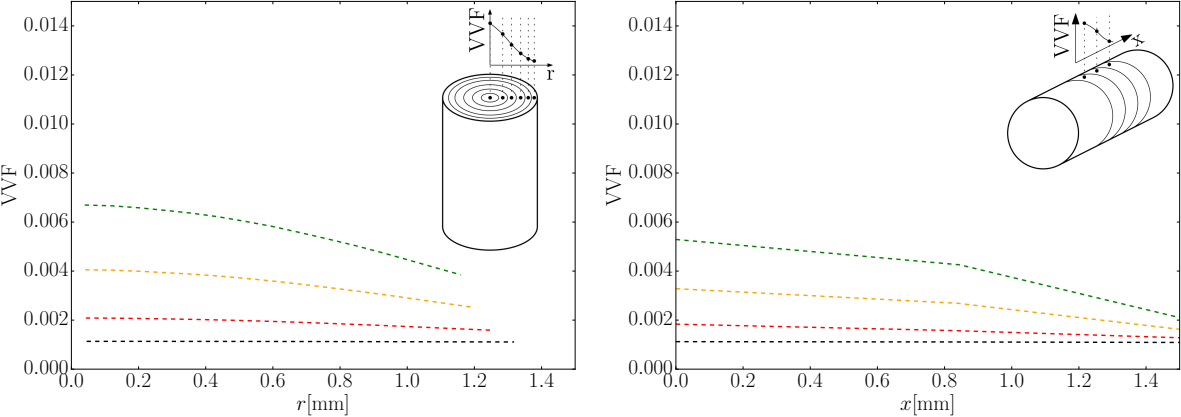
Conflicts of Interest: The authors declare no conflict of interest. The funding sponsors had no role in the design of the study; in the collection, analysis or interpretation of data; in the writing of the manuscript and in the decision to publish the results.

Appendix A. Voids Volume evolution profiles

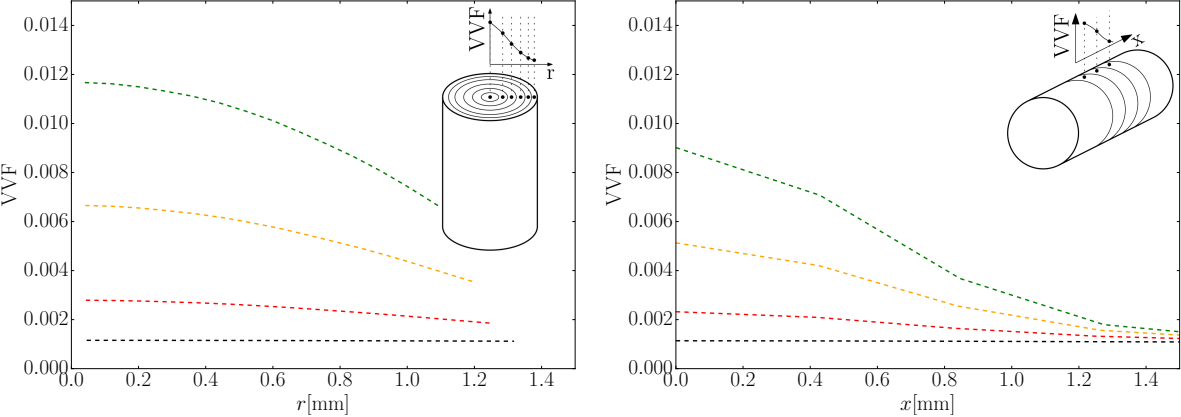
In order to give a glimpse on how radial and longitudinal voids evolution profiles are affected by the longitudinal size of the elements in the numerical model, this appendix shows them for each of the strain stages experimentally analysed using different longitudinal element lengths l , ranging from 0.75 mm. to 0.075 mm.

As in previous figures of the article, black lines are used for step 1, red lines for step 2, yellow for step 3, green for step 4 and blue for step 5.

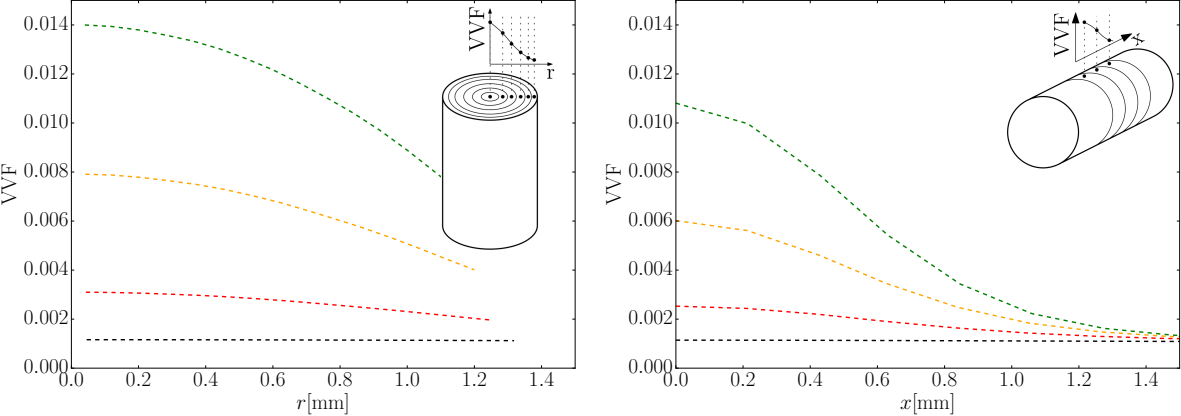
Material 1
a) $l = 0.75\text{mm.}$:



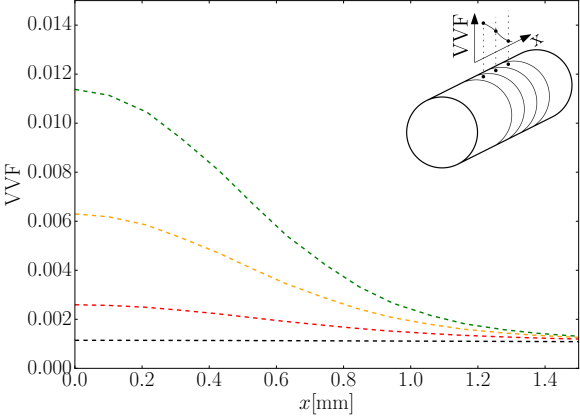
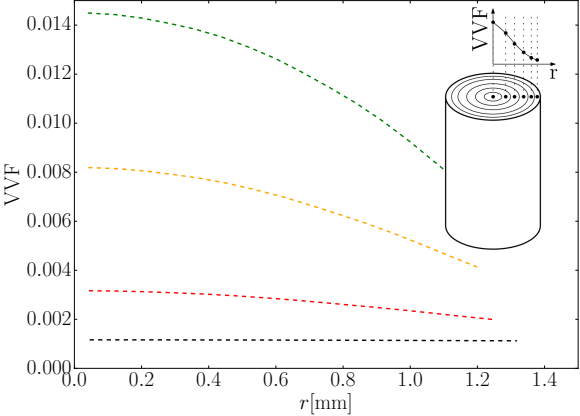
b) $l = 0.375\text{mm.}$:



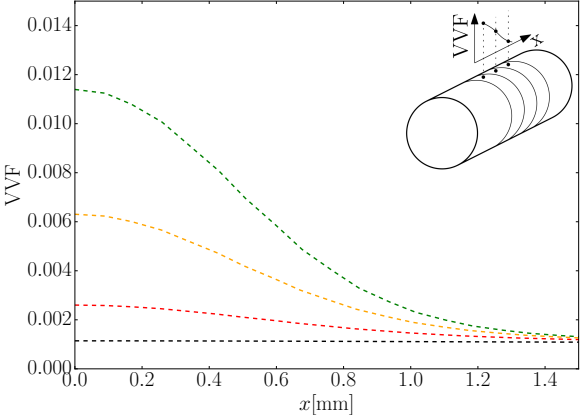
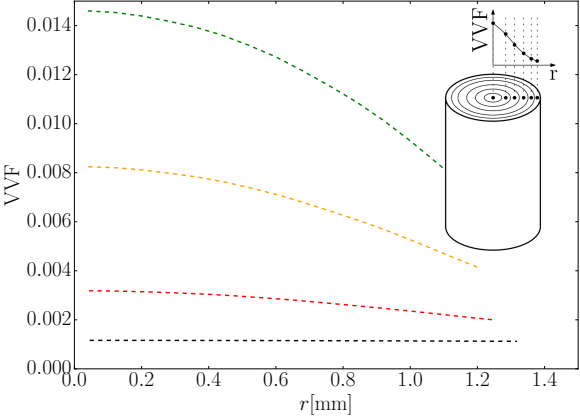
c) $l = 0.188\text{mm.}$:



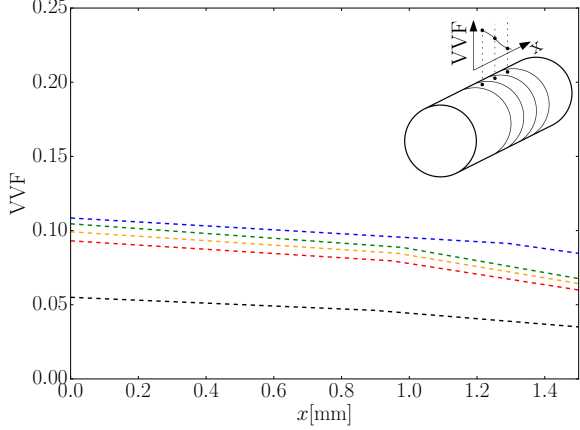
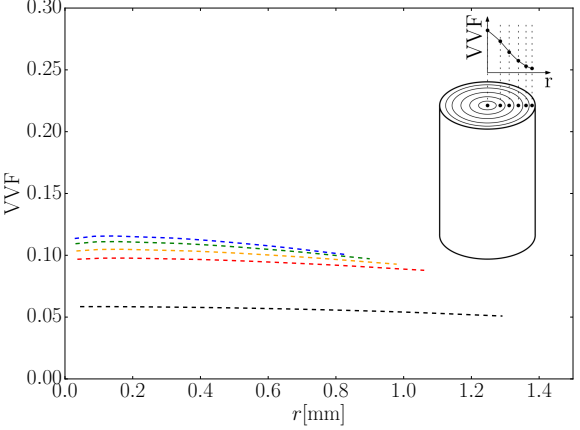
d) $l = 0.095\text{mm.}$:



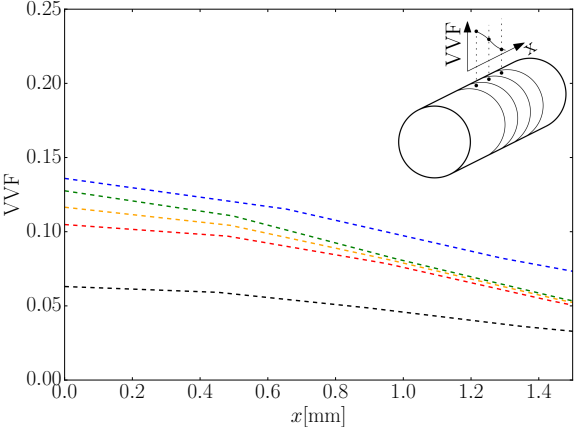
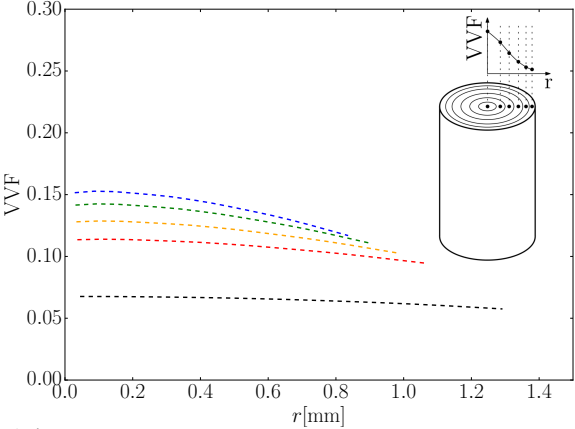
e) $l = 0.075\text{mm.}$:



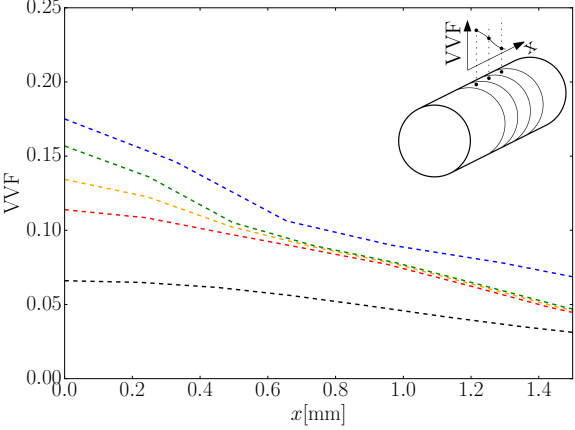
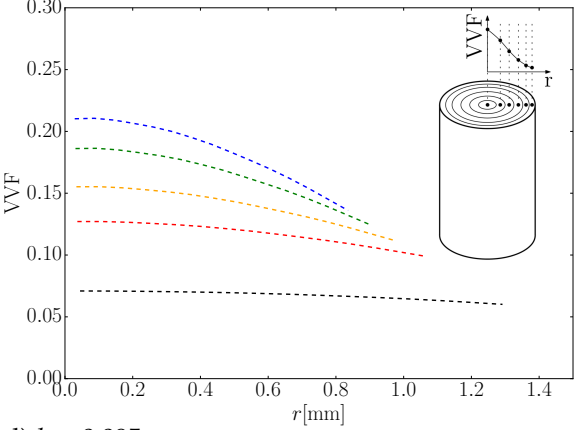
Material 2
a) $l = 0.75\text{mm.}$:



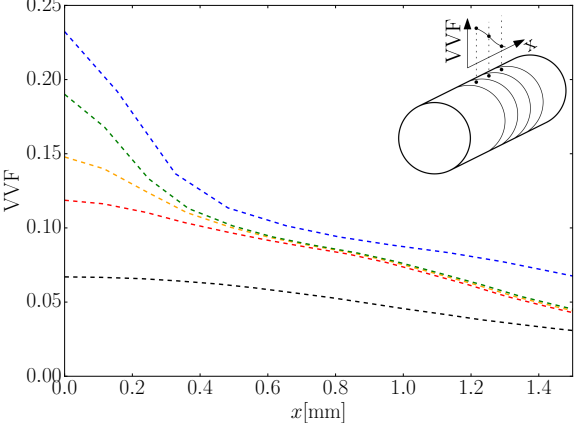
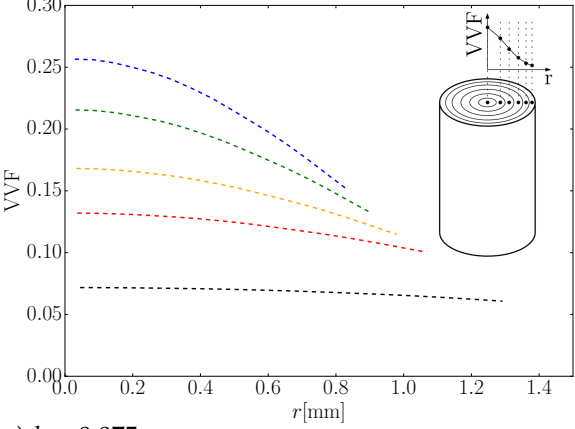
b) $l = 0.375\text{mm.}$:



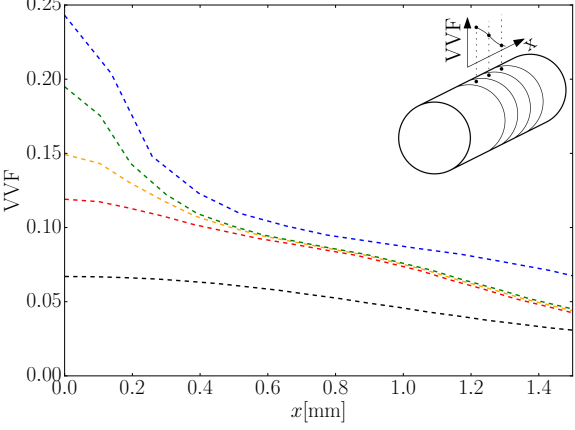
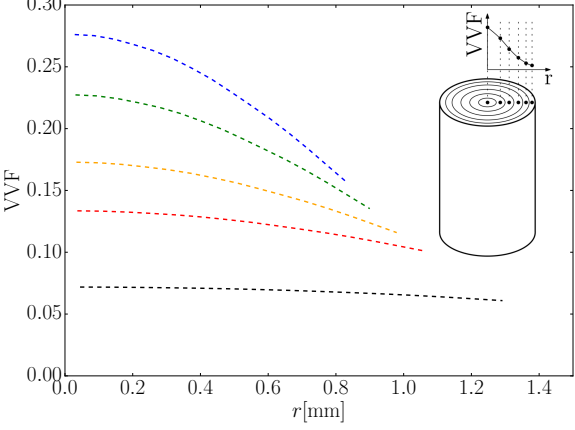
c) $l = 0.188\text{mm.}$:



d) $l = 0.095\text{mm.}$:



e) $l = 0.075\text{mm.}$:



References

1. EN-ISO 6892-1. Metallic materials-Tensile testing-Part 1: Method of test at room temperature. Standard, International Organization for Standardization, 2009.
2. Anderson, T.L.; Anderson, T. *Fracture mechanics: fundamentals and applications*; CRC press, 2005.
3. Gurson, A.L.; others. Continuum theory of ductile rupture by void nucleation and growth: Part I—Yield criteria and flow rules for porous ductile media. *Journal of engineering materials and technology* **1977**, *99*, 2–15.
4. Nègre, P.; Steglich, D.; Brocks, W. Crack extension in aluminium welds: a numerical approach using the Gurson–Tvergaard–Needleman model. *Engineering Fracture Mechanics* **2004**, *71*, 2365–2383.
5. Mirza, M.; Barton, D.; Church, P.; Sturges, J. Ductile fracture of pure copper: An experimental and numerical study. *Le Journal de Physique IV* **1997**, *7*, C3–891.
6. Fei, H.; Yazzie, K.; Chawla, N.; Jiang, H. The effect of random voids in the modified gurson model. *Journal of electronic materials* **2012**, *41*, 177–183.
7. Tvergaard, V.; Needleman, A. Analysis of the cup-cone fracture in a round tensile bar. *Acta metallurgica* **1984**, *32*, 157–169.
8. Suárez, F.; Gálvez, J.C.; Cendón, D.A.; Atienza, J.M. Study of the last part of the stress-deformation curve of construction steels with distinct fracture patterns. *Engineering Fracture Mechanics* **2016**, *166*, 43 – 59. doi:http://dx.doi.org/10.1016/j.engfracmech.2016.08.022.
9. Suárez, F.; Gálvez, J.C.; Cendón, D.A.; Atienza, J.M. Fracture of eutectoid steel bars under tensile loading: Experimental results and numerical simulation. *Engineering Fracture Mechanics* **2016**, *158*, 87 – 105. doi:http://dx.doi.org/10.1016/j.engfracmech.2016.02.044.
10. Maire, E.; Zhou, S.; Adrien, J.; Dimichiel, M. Damage quantification in aluminium alloys using in situ tensile tests in X-ray tomography. *Engineering Fracture Mechanics* **2011**, *78*, 2679–2690.
11. Landron, C.; Maire, E.; Bouaziz, O.; Adrien, J.; Lecarme, L.; Bareggi, A. Validation of void growth models using X-ray microtomography characterization of damage in dual phase steels. *Acta Materialia* **2011**, *59*, 7564–7573.
12. Kahziz, M.; Morgeneyer, T.F.; Mazière, M.; Helfen, L.; Bouaziz, O.; Maire, E. In situ 3D synchrotron laminography assessment of edge fracture in dual-phase steels: quantitative and numerical analysis. *Experimental Mechanics* **2016**, *56*, 177–195.
13. Toribio, J.; Ovejero, E. Effect of cumulative cold drawing on the pearlite interlamellar spacing in eutectoid steel. *Scripta Materialia* **1998**, *39*, 323–328.
14. González, B.; Matos, J.; Toribio, J. Relación microestructura-propiedades mecánicas en acero perlítico progresivamente trefilado. *Anales de Mecánica de la Fractura*, 2009, Vol. 26, pp. 142–147.
15. EN 10020. Definition and classification of grades of steel. Standard, European Committee for Standardization, 2000.
16. Naeimi, M.; Li, Z.; Qian, Z.; Zhou, Y.; Wu, J.; Petrov, R.H.; Sietsma, J.; Dollevoet, R. Reconstruction of the rolling contact fatigue cracks in rails using X-ray computed tomography. *NDT & E International* **2017**, *92*, 199 – 212. doi:https://doi.org/10.1016/j.ndteint.2017.09.004.
17. Garcea, S.; Wang, Y.; Withers, P. X-ray computed tomography of polymer composites. *Composites Science and Technology* **2017**, pp. –. doi:https://doi.org/10.1016/j.compscitech.2017.10.023.
18. Sket, F.; Enfedaque, A.; López, C.D.; González, C.; Molina-Aldareguía, J.; LLorca, J. X-ray computed tomography analysis of damage evolution in open hole carbon fiber-reinforced laminates subjected to in-plane shear. *Composites Science and Technology* **2016**, *133*, 40 – 50. doi:https://doi.org/10.1016/j.compscitech.2016.06.012.
19. MATLAB. *version 8.1.0 (R2013a)*; The MathWorks Inc.: Natick, Massachusetts, 2013.
20. Scheider, I.; Brocks, W. Simulation of cup-cone fracture using the cohesive model. *Engineering Fracture Mechanics* **2003**, *70*, 1943–1961.
21. Bluhm, J.I.; Morrissey, R.J. Fracture in a tensile specimen. Technical report, DTIC Document, 1966.
22. Suárez, F. Estudio de la rotura en barras de acero : aspectos experimentales y numéricos. PhD thesis, Caminos, 2013.
23. Hibbit.; Karlsson.; Sorensen. *ABAQUS/Standard Analysis User's Manual. Version 6.11*; Hibbit, Karlsson, Sorensen Inc.: USA, 2011.
24. Van Rossum, G.; Drake, F.L. *Python language reference manual*; Network Theory, 2003.

25. Ascher, D.; Dubois, P.F.; Hinsén, K.; Hugunin, J.; Oliphant, T.; others. Numerical python, 2001.
26. Jones, E.; Oliphant, T.; Peterson, P. {SciPy}: open source scientific tools for {Python} **2014**.